EXPERIMENTAL AND NUMERICAL SIMULATION OF DISSOLUTION AND PRECIPITATION: IMPLICATIONS FOR FRACTURE SEALING AT YUCCA MOUNTAIN, NEVADA

Patrick F. Dobson[1], Timothy J. Kneafsey, Eric L. Sonnenthal, Nicolas Spycher, John A. Apps

Earth Sciences Division, Lawrence Berkeley National Laboratory, University of California, 1 Cyclotron Road, MS 90-1116, Berkeley, California 94720, USA

Abstract

Plugging of flow paths caused by mineral precipitation in fractures above the potential repository at Yucca Mountain, Nevada, would reduce the probability of water seeping into the repository. As part of an ongoing effort to evaluate thermal-hydrologic-chemical (THC) effects on flow in fractured media, we performed a laboratory experiment and numerical simulations to investigate mineral dissolution and precipitation under anticipated temperature and pressure conditions in the repository. To replicate mineral dissolution by vapor condensate in fractured tuff, water was flowed through crushed Yucca Mountain tuff at 94°C. The resulting steady-state fluid composition had a total dissolved solids content of about 140 mg/L; silica was the dominant dissolved constituent. A portion of the steady-state mineralized water was flowed into a vertically oriented planar fracture in a block of welded Topopah Spring Tuff that was maintained at 80°C at the top and 130°C at the bottom. The fracture began to seal with amorphous silica within five days.

A 1-D plug-flow numerical model was used to simulate mineral dissolution, and a similar model was developed to simulate the flow of mineralized water through a planar fracture, where boiling conditions led to mineral precipitation. Predicted concentrations of the major dissolved constituents for the tuff dissolution were within a factor of 2 of the measured average steady-

[1] Correspondence should be addressed to Patrick Dobson (pfdobson@lbl.gov; fax (510) 486-6115)

state compositions. The mineral precipitation simulations predicted the precipitation of amorphous silica at the base of the boiling front, leading to a greater than fifty-fold decrease in fracture permeability in 5 days, consistent with the laboratory experiment.

These results help validate the use of a numerical model to simulate THC processes at Yucca Mountain. The experiment and simulations indicated that boiling and concomitant precipitation of amorphous silica could cause significant reductions in fracture porosity and permeability on a local scale. However, differences in fluid flow rates and thermal gradients between the experimental setup and anticipated conditions at Yucca Mountain need to be factored into scaling the results of the dissolution/precipitation experiments and associated simulations to THC models for the potential Yucca Mountain repository.

Key words: Dissolution, precipitation, porosity, permeability, reactive transport, heat pipe

1. Introduction

The emplacement of heat-generating nuclear waste in a potential geologic repository at Yucca Mountain, Nevada, would enhance water-rock interaction around the emplacement drifts. As the waste heats the surrounding environment, water present in the rock matrix and fractures would vaporize and migrate through fractures to cooler regions where condensation would occur. The condensate would dissolve gases and minerals, and mineralized water flowing under gravity back towards the repository would evaporate, depositing the dissolved minerals. This mineral deposition would reduce porosity and permeability above the potential repository, thus altering the flow paths of percolating water (Nitao and Glassley, 1999).

The effects of tuff dissolution and precipitation in fractures have been studied by others. Johnson et al. (1998) conducted a plug-flow dissolution experiment to validate the GIMRT code

with dissolution of granular tuff and quartz in deionized water at 84 bars and 240°C, conditions far outside the range expected for the potential Yucca Mountain repository. Moore et al. (1986) observed limited permeability changes in an experiment in which water was forced through a hollow cylinder of nonfractured tuff under a temperature gradient; the minimal reduction in permeability was interpreted to be due to the high initial tuff-matrix porosity. In another experiment, the permeability of saw-cut and natural fractures, when submitted to flowing water and steam at increased temperature, decreased continuously, particularly at temperatures exceeding 89°C (Daily et al., 1987, Lin and Daily, 1989). Rimstidt et al. (1989) constructed a heat pipe in a column of tuff chips, consisting of a superheated region where boiling occurred, a nearly isothermal liquid-vapor counterflow region, and a cooler region where condensation occurred. After 30 days, the experiment resulted in a zone of dissolution where condensation occurred, overlying a counterflow region (where little change took place), which in turn overlay a zone where obvious cementation of the tuff grains occurred. All of these experiments demonstrated that interaction of water and ash flow tuff can result in mineral dissolution and precipitation.

In this work, we experimentally examined mineral dissolution, precipitation, and associated changes in porosity and permeability to replicate chemical reactions occurring within a heat pipe. The first experiment examined tuff dissolution at conditions similar to those expected near a high-level nuclear waste repository situated in unsaturated tuff (e.g., the condensation end of a heat pipe). This experiment differs from the experiment reported by Johnson et al. (1998) in that the temperature, pressure, and chemical conditions of our work more closely replicate those expected around the potential repository. The second experiment explored the consequences that boiling of a mineralized fluid would have on fracture porosity and permeability, as would occur

at the boiling end of a heat pipe. At Yucca Mountain, the boiling region would be close to the heated repository drifts, whereas condensation would occur farther away where the rock would be cooler. The well-constrained experimental conditions formed the basis for coupled-process simulations using the TOUGHREACT code (Xu and Pruess, 1998, 2001a, b; Sonnenthal and Spycher, 2001), providing a benchmark for numerical model validation. This work illustrates the potential for fracture sealing caused by the reflux of fluids that undergo boiling, condensation, tuff dissolution, and subsequent boiling and mineral precipitation.

2. Experimental Approach

2.1. Tuff Dissolution

We dissolved devitrified welded rhyolite ash flow tuff (Figure 1) from the Topopah Spring Tuff (middle nonlithophysal zone) of the Paintbrush Group in a plug flow reactor, using a similar approach to that of Johnson et al. (1998). The rock sample used for the tuff dissolution experiment was obtained from the Single Heater Test rock block in the Exploratory Studies Facility (ESF) at Yucca Mountain, Nevada. The fragments contained a sealed fracture and no lithophysal cavities. Using distilled water as a proxy for condensate, the fluid was equilibrated with 50,200 ppm CO_2. Dissolved CO_2 was added because similar CO_2 concentrations have been detected in Drift-Scale Test gas samples due to exsolution of the gas from the matrix water (Sonnenthal and Spycher, 2001). The tuff was crushed, sieved, and washed using an ultrasonic bath to obtain a fairly uniform grain size distribution, with 89% of the tuff derived from the 75–150 μm sieve fraction and the remaining 11% from the 150–212 μm sieve fraction. SEM images of the crushed tuff indicate rough, irregular grains, with the actual size distribution appearing to be shifted to slightly smaller sizes (30–180 μm). The crushed tuff was packed into a

polypropylene vessel 7.5 cm in diameter and 29.8 cm in length, with a porosity of 37.5%. The mineralogy of this tuff is presented in Table 1.

The plug flow column was kept in an oven maintained at 94°C and atmospheric pressure, and water was flowed through the crushed tuff at 25 mL/h for 1,530 hours and collected in a reservoir in the oven. This reservoir was regularly sampled and analyzed for silica, aluminum, calcium, iron, sodium, potassium, fluoride, chloride, nitrate, sulfate, total alkalinity, electrical conductivity, and pH. Cations and silica were measured using inductively coupled plasma–atomic emission spectrometry, and anions were analyzed using ion chromatography. Electrical conductivity was measured with a Cole-Parmer Electrical Conductivity Meter, alkalinity was determined using titration, and pH was measured using a Cole-Parmer pH/mV/°C meter.

2.2. Mineral Precipitation and Fracture Sealing

Effluent from the tuff dissolution column was flowed through a heated fracture to emulate the reflux of condensate back through a fracture network and into a boiling environment. After steady-state conditions were attained in the plug-flow reactor, a portion of the water generated from the reactor was flowed at 10.8 mL/h into the top of a 31.7 cm tall, 16.2 cm wide, vertically oriented planar (saw-cut) fracture between two 3.2 cm thick welded devitrified rhyolite ash flow tuff blocks. The blocks of Topopah Spring Tuff contained a small fracture and no lithophysal cavities, and were obtained from Alcove 6 in the ESF at Yucca Mountain. The outer surfaces of the rock were sealed with Dow Corning 1199 silicone, and the vertical sides of the fracture were sealed with an aluminum sheet covered with DC 1199 silicone. Polypropylene endcaps were manufactured to fit the assembly, sealed with DC 1199 silicone, and held in place using stainless steel bands. Vapor exiting the base of the fracture assembly was condensed, collected, and analyzed.

The dimensions of the fracture and the temperature gradient were selected based on relations derived by Phillips (1994, 1996), Darcy's law, and the cubic law. A saw-cut fracture was selected because the geometry was simple (planar) and the mineralogy of the fracture surfaces was the same as that of the matrix. The two blocks were separated with 17.7 μm gold shims; however, the hydraulic aperture calculated using the initial measured air permeability of the fracture and the cubic law (permeability = aperture^2/12) was about 31 μm. This aperture difference was attributed to surface roughness and a slight waviness in the ground-flat rock surfaces.

Tuff block heating was accomplished using electrical resistance heaters mounted on the sides of the blocks to establish a temperature of 80°C at the top and 130°C at the bottom. Temperatures were monitored throughout the duration of the experiment with a series of thermocouples located at 2.7, 7.1, 11.5, 15.9, 20.3, 24.7, and 29.1 cm from the rock bottom, and 0.6 cm from the fracture surface.

3. Modeling Approach

3.1. Numerical Simulators

The TOUGHREACT simulator (Xu and Pruess, 1998, 2001a, b; Sonnenthal and Spycher, 2001) was used for the present calculations. TOUGHREACT incorporates reactive chemistry and transport into the framework of the TOUGH2 code, which simulates multiphase flow of gas and fluids together with tracer and heat transport through porous and/or fractured geologic media (Pruess, 1991). TOUGHREACT uses a sequential iteration approach for coupling chemical transport and reaction. After solution of the flow equations, the fluid velocities and phase saturations are used for chemical transport simulation. Chemical transport is solved on a

component basis, and the resulting concentrations are substituted into the chemical reaction model. The system of chemical reaction equations is solved on a gridblock basis by Newton-Raphson iteration. For all simulations, the equation of state module EOS3 was used, which considers the fully coupled flow of water, air, and heat.

The TOUGHREACT code allows for the selection of either kinetic or equilibrium thermodynamics to be used for mineral dissolution and precipitation. An affinity-limited kinetic rate law (Steefel and Lasaga, 1994) employing geometric surface areas and no pH dependence was used for the kinetic calculations. A slightly modified form of this rate law was used to model amorphous silica precipitation (Carroll et al. 1998). An extended form of the Debye-Hückel equation was used to approximate ion activity coefficients at elevated fluid salinities (Helgeson et al., 1981). Under conditions when grid blocks that receive fluxes of water (and dissolved constituents) boil away completely prior to the solution of the chemical mass balance equations, mineral precipitation was calculated using a normative method, where phases were sequentially formed using stoichiometric compositions. For the fracture-sealing simulations, porosity changes resulting from mineral dissolution and precipitation were used to calculate corresponding changes in permeability by employing the cubic law relation between porosity and permeability. Two thermodynamic databases were employed for the simulations: thermokapps2.05.dat and thermok2.07.dat (Sonnenthal and Spycher, 2001). Rate constants for kinetic reactions that were appropriate for near-neutral pH conditions were chosen, consistent the range of pH values observed in the experiment.

3.2. Simulation of Tuff Dissolution

A 149-element horizontal 1-D mesh with overall dimensions and interface areas identical to the tuff dissolution reactor experiment was constructed for use in the simulations. Each of the

blocks had a width of 2 mm. An additional boundary element with a very large volume (>10^{50} m^3) was added to the end of the column to serve as a constant pressure boundary, thus preventing excess fluid pressure from forming. The initial mineralogy used for the plug-flow simulations is presented in Table 1.

The column was assumed to be liquid-saturated. The maximum time step per element block (360 seconds) was selected to be smaller than the liquid residence time of 477 seconds calculated from the column experiment. The temperature and pressure of the simulation were fixed at 94°C and 1 bar, respectively. The initial fluid bicarbonate composition (HCO_3^- = 1.943 × 10^{-3} M) was calculated using the code SOLVEQ v.1.0 (Reed, 1982; Spycher and Reed, 1992) and the measured pH (4.58) and pCO_2 (0.0502 bars). Trace amounts of other dissolved constituents (1.0 × 10^{-10} M) were used in the simulation to reduce computational problems caused by zero values.

3.3. Simulation of Mineral Precipitation and Fracture Sealing

A series of one-dimensional multiple continuum simulations were performed to model fracture sealing using a mesh configuration with dimensions identical to those in the tuff fracture experiment. Assuming symmetry, only half of the system was modeled. The mesh design contains two columns of rock blocks and one column of fracture blocks, with each column consisting of 317 elements with a uniform height of 1 mm. The outermost rock column consists of elements with fixed temperatures to approximate the experimental temperature gradient (80–130°C). The simulations had a maximum time step of 0.333 seconds. Fluid was injected into the uppermost fracture element, while the lowermost fracture element was assigned a very large (>10^{50} m^3) volume to act as a constant pressure and temperature boundary. The injected fluid

composition was taken from the measured average values obtained from the tuff dissolution experiment, and the initial rock mineralogy was considered to be the same as that used for the plug-flow experiment (Table 1). The initial fracture permeability was set to the experimental conditions, while the flow rate and fracture width were reduced by half (5.4 mL/h and 15.5 μm, respectively) to account for the assumption of symmetry. To simplify the simulation, the rock matrix blocks were assigned a zero permeability to force the injected water to flow through and interact only with the fracture elements, and thus the matrix elements served only as a heat transport mechanism. Different simulations were run with amorphous silica (the main precipitating phase in the fracture zone) controlled by either equilibrium (Rimstidt, 1997) or kinetic (Carroll et al., 1998) conditions.

4. Results

4.1. Tuff Dissolution Experiment

The concentrations for all dissolved components initially increased rapidly, and then declined until about 230 hours, after which relatively steady concentrations were achieved (Figure 2). The high initial concentrations may have resulted from the dissolution of fine tuff particles not removed in the washing process, which resulted in a much higher available reactive surface area at the start of the experiment, or from the initial mineral surfaces being more reactive because of crushing and surface roughness. Average steady-state aqueous concentrations of the predominant measured species leaving the tuff dissolution column are shown in Table 2. The resulting steady-state fluid composition had a total dissolved solids content of about 140 mg/L; silica (92 mg/L) was the dominant dissolved constituent. The effluent was supersaturated with respect to quartz (55 ppm SiO_2), but was undersaturated with respect to α-cristobalite (114 ppm)

and amorphous silica (350 ppm). The fluid compositions underwent a large shift in pH from the initial value of 4.58 to a steady-state value of 8.4. While part of the shift in pH resulted from water-rock interaction, cooling and degassing of the effluent after entering the fluid reservoir and prior to analysis were in part responsible for elevated pH.

A simple mass-balance calculation using the steady-state fluid composition of the reactor effluent (omitting bicarbonate), the amount of fluid flowed through the column, and the duration of fluid flow resulted in an estimated total of 4.1 g of rock dissolved. Using the initial amount of tuff loaded in the column (1840 g), a total of 0.22 wt.% of the tuff was dissolved over the duration of the experiment.

4.2. Tuff Dissolution Simulations

Five tuff dissolution simulations were performed (Tables 2 and 3). The first two simulations employed two different grain-size models to evaluate the sensitivity of the surface area values on kinetic mineral reactions. Because the grains used in the experiment are rock particles that consist mainly of composite mineral grains, the following grain-size models are used to approximate reactive surface areas for each mineral present, and are not meant to describe the actual grain size of the mineral phases. Simulation 1 employed mineral surface areas of 394 cm^2/g (for all minerals except clays) and 6824 cm^2/g (clays). These values were calculated using spherical grains with a diameter of 60 μm for the non-clay minerals, and using rectangular plates having the dimensions 60 × 60 × 1.2 μm for clay minerals. Simulation 2 used mineral surface areas of 197 and 3412 cm^2/g (spherical grains 120 μm diameter, clay minerals 120 × 120 × 2.4 μm). Differences up to 100% were observed between the two grain-size models for Na, SiO_2, and Ca concentrations (Figure 2). These differences resulted from the two-fold difference in

calculated initial surface areas, which affect the kinetic mineral reactions controlling the concentrations of these species in solution. There is a close match between the measured and calculated concentrations of Na and SiO_2 for Simulation 1 (Figure 2 and Table 2).

The closer correspondence of the fluid chemistry data to the smaller grain-size surface area model is not surprising on several counts. First, while the sieve grain fractions for the tuff suggest that the average grain size is more in keeping with the 120 μm diameter model, the SEM images clearly show that smaller diameter particles are present. The simple geometric models also used a spherical grain shape for most minerals, which would tend to underestimate the actual surface area/unit weight value. This is because grains with irregular shapes, rough surfaces, and internal porosity would have larger surface area/unit weight values that are more closely approximated by the 60 μm grain size model. As a result, the surface areas corresponding to the 60 μm grain size model were used in all subsequent simulations.

Simulations 3–5 were conducted using temperature- and pressure-corrected density values of water in surface-area calculations. These values result in a small change in calculated surface areas for the new series of simulations (Sonnenthal and Spycher, 2001). These simulations also varied the thermodynamic properties of some of the mineral phases. Simulation 3 used an ideal solid-solution model for Na-Ca-Mg smectite and ignored the small fraction of K-smectite. Simulation 4 used the same scheme to model smectite, but used a slightly less stable potassium feldspar phase than used in Simulations 1–3 (Sonnenthal and Spycher, 2001). Simulation 5 was similar to Simulation 4, with the exception that the K-smectite fraction was added to the illite fraction.

From our simulations, we note that Simulations 3–5 produced results similar to those of Simulation 1 (each of which employed the same 60 μm grain-size model). Most of the

concentration profiles for Simulations 3–5 have steady-state compositions that are slightly (~5%) higher than the corresponding values of Simulation 1, resulting from the incorporation of the change in water density to the mineral surface area calculations in Simulations 3–5. Changes made in the choice of thermodynamic parameters for potassium feldspar resulted in significant changes in the simulated K^+ concentrations (as well as slightly higher silica concentrations) for Simulations 4 and 5. It is, therefore, critical to select the proper thermodynamic data for the key mineral phases that buffer the main chemical constituents in the fluid.

Changes in mineralogy resulting from water-rock interaction in the tuff occurred for each of the simulations. Most of the phases initially present (feldspars, silica polymorphs, and the smectite minerals) underwent dissolution throughout the course of the simulated experiment, with albite and anorthite being the main dissolved phases. While potassium feldspar was dissolved throughout the first half of the tuff column, it precipitated within the second (outlet) half. Illite underwent dissolution only in the vicinity of the column inlet and was precipitated throughout the remainder of the column; this is consistent with the insensitivity of the runs to small changes in initial illite abundance (Simulations 4 and 5). Kaolinite was the main phase precipitating in the reactor column. The column underwent an overall decrease in mineral volume with time. The simulated decrease of 0.17 vol. % for Simulation 3 is similar to the decrease of 0.22 wt. % calculated for the experiment.

The simulation results do not match the measured values of pH and total alkalinity. The discrepancy in pH can be attributed to the exposure of the plug-flow effluent to air and the subsequent cooling and degassing of the outflow prior to analysis. The simulated water composition for Simulation 1 was subjected to equilibration with air and cooling using SOLVEQ v1.0. The simulated output composition was first equilibrated with a pCO_2 of $10^{-3.5}$ bar

(approximately the atmospheric pCO_2) and charge balancing the solution using HCO_3^-. A second adjustment was made by cooling the solution from 94°C to 20°C. The first step resulted in an increase in pH from 6.07 to 8.33, while cooling the solution resulted in a small drop in pH to 8.08. The corrected pH is very close to the measured laboratory value of 8.2.

4.3. Mineral Precipitation and Fracture Sealing Experiment

After five days, the approximately 31 μm aperture planar fracture began to seal. Sealing was indicated by a declining outflow rate and leaks in the inlet side of the fracture. Pre-experiment modeling indicated that fracture sealing was not expected so early in the experiment; consequently, the leaks were plugged and continued flow was attempted. Increased pressure was required to maintain the flow of water at 10.8 ml/hr following the onset of fracture sealing. After several unsuccessful attempts to plug leaks and the near-zero rate of effluent collection, it was concluded that the aperture was effectively sealed.

Following cooling, the fracture was opened to examine the precipitate location (Figure 3) and morphology. The precipitate (identified as mainly amorphous silica from SEM X-ray analyses and visual and petrographic examination) was deposited almost exclusively at temperatures exceeding the boiling point; however some precipitation occurred in the sub-boiling region. The morphology of the precipitate differed with the temperature at which precipitation occurred. Fine-textured grainy precipitate occurred in a few locations in the sub-boiling region. This precipitate had little effect on fracture permeability. Near 100°C, precipitate formed solid, well-formed bridging structures, in addition to some coating the fracture walls (Figure 4). At temperatures near 110°C, wall-coating precipitate having vitreous luster with bridging structures was deposited. In the lowest and hottest regions (~120°C), very porous, veiny, honeycomb-like bridging structures were formed. Any deposition on the fracture walls would tend to plug

microfractures and pores, thus reducing the permeability into the rock from the fracture. Similar morphologies for secondary opal-A deposited on fracture and borehole surfaces were noted at the Single Heater Test site at Yucca Mountain (Cho, 1999).

Aperture sealing occurred after 5 days with only a relatively small fraction (1.2–4.7%) of the total fracture porosity filled with solid precipitate, primarily composed of amorphous silica. These estimates are based on dividing the total volume of dissolved solids (precipitated) carried by (1) the total volume of effluent collected and (2) the total amount of water injected into the top of the fracture, by the initial fracture volume. The discrepancy between the measured amounts of input water and outflow fluid results from leakage occurring during the later stages of the experiment when fracture permeability was greatly reduced and filling of matrix porosity of the rock blocks.

4.4. Mineral Precipitation and Fracture Sealing Simulation

The results of these simulations indicated the formation of a nearly isothermal region (Figure 5), with an overlying water column above and a vapor zone below. The precipitation of amorphous silica at the base of the nearly isothermal two-phase zone accounted for all of the porosity and permeability reduction in the fracture system. A gradual buildup in pressure, caused by the reduction in the fracture aperture, occurred at the top of the fracture system, resulting in a corresponding downward shift of the base of the boiling zone over time. Silica precipitation and porosity reduction followed the boiling front downward, spreading the effects of boiling and concomitant mineralization.

The thickness and location of the mineralized zone varied between kinetic and equilibrium simulations (Figure 6). The simulations conducted using equilibrium precipitation and dissolution controls for amorphous silica (i.e., Simulation A) showed the effects of both

precipitation and dissolution, as the trailing edge of the silica front underwent dissolution with time. For the kinetic simulations (Simulation B), almost no dissolution of precipitated amorphous silica occurred, resulting in a thicker band of silica precipitation that occluded less of the fracture aperture, so that the sealing zone did not extend as far down the fracture as in the equilibrium case. The maximum porosity and permeability reduction (for a given fracture element) were greater for the equilibrium simulations (Simulation A), with 80% porosity reduction and a permeability reduction of >99% over the 5.8 day duration of the simulations. The kinetic simulation (Simulation B) had porosity and permeability reductions of 70% and 97%, respectively.

Significant permeability reduction occurred in the simulations within 5 days after the initiation of fluid flow for both the experiment and the simulations. The presence of silica precipitate throughout the boiling zone in the experiment suggests that the kinetic simulation (which retains early-formed precipitate) is a more appropriate match to the experimental results. Some of the differences between the experiment and the simulations may result from variability in the two-dimensional fracture surface in the experiment, as well as from fluctuations resulting from fluid leaks and a short-term power outage that occurred during the experiment.

5. Applicability of Dissolution/Precipitation Experiments and Simulations to Yucca Mountain: Scaling Effects

It is important to compare differences in scale between the laboratory experiment and associated simulations with predicted conditions for the potential Yucca Mountain repository. To address the rate of possible fracture sealing for the Yucca Mountain system, the following

factors must be considered when applying the experimental results to the near-field environment of the potential repository:

- Water flow rate in fractures (reflux of water via heat pipe effect)
- Fracture porosity, apertures and geometry
- Thermal gradient and thickness of boiling front and condensation zone
- Mobility of boiling front with time
- Fracture-matrix interaction
- Effective mineral surface area in condensation zone

The key differences between the Yucca Mountain system and the experiment (Table 4) are fracture flow rates (fracture fluid flux) and the width of the boiling zone (gradient). If we assume that simple linear scaling is adequate to obtain a rough estimate of the time frame in which fracture sealing could be expected at Yucca Mountain, then we can scale the time by the ratios of these parameters. Assuming that the width of the boiling front over which silica precipitation occurs can be represented approximately by the thermal gradient, then the time required for fracture sealing (plugging) at Yucca Mountain can be estimated as

$$Time_{YM} = (Time_{EXP})\left(\frac{FluidFlux_{EXP}}{FluidFlux_{YM}}\right)\left(\frac{Gradient_{EXP}}{Gradient_{YM}}\right)\left(\frac{Aperture_{YM}}{Aperture_{EXP}}\right)\left(\frac{Concentration_{EXP}}{Concentration_{YM}}\right)$$

where YM indicates Yucca Mountain and EXP indicates the experiment. Using the values from Table 4, we obtain

$$Time_{YM} = (5\,days)\left(\frac{6\times10^{-4}\,m/s}{3\times10^{-7}\,to\,3\times10^{-8}\,m/s}\right)\left(\frac{158^{\circ}C/m}{0.75^{\circ}C/m}\right)\left(\frac{10\,to\,1000\,\mu m}{31\,\mu m}\right)\left(\frac{92\,mg/l}{58\,to\,139\,mg/l}\right)$$

which provides us with sealing times for Yucca Mountain ranging from 10^3 years for the high-flow, high concentration, small aperture condition, to nearly 3×10^6 years for the low flow, low concentration, large aperture condition. Shorter sealing times would be obtained for Yucca Mountain if reflux of fluids is considered, and if the zone of silica deposition is not broadened by the lower thermal gradient. The lower estimated rate of fracture sealing is within the range of values obtained by Nitao and Glassley (1999), whose THC simulations for the potential Yucca Mountain repository (calculated using a fracture porosity of only 0.01%) predict that a porosity reduction of greater than 90 percent for the area 6 m above the drifts will occur 1,500 to 4,000 years after waste emplacement if boiling conditions persist that long. Much longer sealing times are predicted to occur for larger aperture fractures using this simplistic linear scaling relation. The importance of fracture aperture on sealing indicated by this model is consistent with THC modeling results for the potential Yucca Mountain repository obtained using a heterogeneous fracture model (BSC, 2001; Section 4.3.6).

The processes controlling the rate of fracture plugging are more complex than this simple scaling calculation. The mineralogy, effective mineral surface area, and temperature control the amount of silica that can dissolve in the condensate. The rate of downward fluid flow from the condensation zone to the boiling zone serves as a limiting factor to the amount of silica transport and resulting mineralization that can occur in the fractures. Our scaling model also only considers a static boiling zone. A mobile boiling zone (which would be expected for the Yucca Mountain system) would result in longer sealing times because silica precipitation would occur over a larger area.

Water flow at Yucca Mountain is controlled by several factors, such as surface infiltration rates (which vary on regional and climatic scales) and focused flow along high permeability

faults and fractures, and will be influenced by reflux of fluids associated with condensation above the drift zones. Localized zones with elevated flow rates within the boiling front would be most susceptible to silica self-sealing; however, if flow is adequate, these are also the most likely to penetrate the dryout zone. Fracture geometry affects sealing by controlling flow paths to locally narrow apertures. As the results of the experiment and simulations indicate, only small amounts of total porosity reduction (via mineralization) are required along sharp, stationary boiling fronts and within narrow apertures to seal a fluid conduit. The location of flow pathways in unsaturated fractures is influenced by the local permeability structure of the fracture, capillary forces, and the flow itself. First-generation fracture sealing is likely to occur at the perimeter of flowing fingers where the aperture is narrow. Later-generation flows might then be forced into regions where the aperture is wider and viscous flow buffering is reduced. These flows might then have higher velocities and possibly penetrate deeper into the dryout zone.

6. Conclusions

Fracture sealing can occur under conditions in which boiling fluids deposit dissolved silica. Narrowing of the aperture reduces fracture permeability, but aperture narrowing over a small zone may be adequate to seal the fracture to water flow. Using TOUGHREACT, we were able to obtain a good match between the water compositions for the observed and simulated plug flow reactions. The simulations were sensitive to a number of parameters, including the initial mineral assemblage, the thermodynamic parameters used, and (most importantly) the mineral surface area.

TOUGHREACT models of fracture fluid flow involving boiling and precipitation of dissolved constituents resulted in simulated porosity and permeability changes that are similar to

those observed in the experiment, with significant permeability reduction occurring after 5 days. Kinetic control of amorphous silica appears to more closely approximate the observed distribution of silica along the fracture than equilibrium control.

The results of the experiment and simulations can be used to provide bounding estimates for the time required for fracture sealing associated with condensing and boiling fluids above heated drifts at the potential repository at Yucca Mountain. Because of the large difference in fluid flux rates and thermal gradients, fracture sealing at the potential Yucca Mountain repository is estimated to require much longer periods of heat pipe activity (10^3 to 3×10^6 years) than the laboratory experiment. This amount of time is typically longer than the time that boiling temperatures are predicted to exist for the high-temperature thermal load configuration (1000–2000 years), and thus fracture sealing is not predicted to occur in general. Fracture sealing could occur in small aperture fractures and in localized areas where fluid flux rates are much higher, due to focussed flow and reflux of condensate.

Acknowledgments

Support and useful discussions helping guide this work were provided by Liviu Tomutsa, H. Scott Mountford, Thana Alusi, Andrew Mei, David Anderson, Karsten Pruess, Stefan Finsterle, Peter E. Persoff, Ardyth Simmons, Bo Bodvarsson, and Ernest L. Hardin. Helpful reviews of this work were provided by Tianfu Xu, Yongkoo Seol, Dan Hawkes, Hari Viswanathan, and David Vaniman. This work was supported by the Director, Office of Civilian Radioactive Waste Management, U.S. Department of Energy, through Memorandum Purchase Order EA9013MC5X between Bechtel SAIC Company, LLC and the Ernest Orlando Lawrence Berkeley National Laboratory (Berkeley Lab). The support is provided to Berkeley Lab through the U.S. Department of Energy Contract No. DE-AC03-76SF00098.

References

BSC (Bechtel SAIC Company), 2001. FY 01 Supplemental Science and Performance Analyses, Volume 1: Scientific Bases and Analyses. TDR-MGR-MD-000007 REV00 ICN 01. Bechtel SAIC Company, Las Vegas, Nevada.

Carey, T.W., 2000. Mineralogical Model (MM3.0), MDL-NBS-GS-000003 REV00 ICN01. CRWMS M&O, Las Vegas, Nevada.

Carroll, S., Mroczek, E., Alai, M. and Ebert, M., 1998. Amorphous silica precipitation (60 to 120°C): Comparison of laboratory and field rates. Geochim. Cosmochim. Acta, 62: 1379-1396.

Cho, J.B., 1999. Single Heater Test Final Report, BAB000000-01717-5700-00005 REV 00 ICN 01. Civilian Radioactive Waste Management System Management and Operating Contractor (CRWMS M&O), Las Vegas, Nevada.

Daily, W., Lin, W. and Buscheck, T., 1987. Hydrological Properties of Topopah Spring Tuff: Laboratory Measurements. J. Geophys. Res., 92(B8): 7854–7864.

Freifeld, B.M., 2001. Estimation of fracture porosity in an unsaturated fractured welded tuff using gas tracer testing. Ph.D. thesis, University of California, Berkeley, California.

Helgeson, H.C., Kirkham, D.H. and Flowers, G.C., 1981. Theoretical prediction of the thermodynamic behavior of aqueous electrolytes at high pressures and temperatures. IV. Calculation of activity coefficients, osmotic coefficients, and apparent molal and standard and relative partial molal properties to 600°C and 5 kb. Am. J. Sci., 281: 1249-1536.

Johnson, J.W., Knauss, K.G., Glassley W.E., DeLoach, L.D. and Tompson, A.F.B., 1998. Reactive transport modeling of plug-flow reactor experiments: Quartz and tuff dissolution at 240°C. J. Hydrol., 209: 81–111.

Lin, W. and Daily, W.D., 1989. Laboratory Study of Fracture Healing in Topopah Spring Tuff - Implications for Near Field Hydrology. UCRL–100624, Lawrence Livermore National Laboratory, Livermore, California.

Moore, D.E., Morrow, C.A. and Byerlee, J.D., 1986. High-temperature permeability and groundwater chemistry of some Nevada Test Site tuffs. J. Geophys. Res., 91(B2): 2163–2171.

Nitao, J.J. and Glassley, W.E., 1999. Modeled near-field environment porosity modification due to coupled thermohydrologic and geochemical processes. Proceedings, Scientific Basis for Nuclear Waste Management XXII, Materials Research Society, 556, Warrendale, Pennsylvania, pp. 705–711.

Phillips, O.M., 1994. Liquid infiltration through the boiling point isotherms in a desiccating fractured rock matrix. Proceedings, Fifth International High-Level Radioactive Waste

Management Conference, American Nuclear Society, American Society of Civil Engineers, Las Vegas, Nevada: 2189–2196.

Phillips, O.M., 1996. Infiltration of a liquid finger down a fracture into superheated rock. Water Resour. Res., 32: 1665–1670.

Pruess, K., 1991. TOUGH2—a general-purpose numerical simulator for multiphase fluid and heat flow. Rep. LBL–29400, Lawrence Berkeley National Laboratory, Berkeley, California.

Reed, M.H., 1982. Calculation of multicomponent chemical equilibria and reaction processes in systems involving minerals, gases, and an aqueous phase. Geochim. Cosmochim. Acta, 46: 513–528.

Rimstidt, J.D., 1997. Quartz solubility at low temperatures. Geochim. Cosmochim. Acta, 61: 2553-2558.

Rimstidt, J.D., Newcomb, W.D. and Shettel, D.L., Jr., 1989. A vertical gradient experiment to simulate conditions in vapor dominated geothermal systems, epithermal gold deposits, and high level radioactive repositories in unsaturated media. In: Proceedings of the 6th International Symposium on Water-Rock Interaction, WRI-6, Malvern, United Kingdom, 3–8 August 1989, Miles, D.L., ed., A.A. Balkema, Rotterdam, The Netherlands, pp. 585–588.

Sonnenthal, E. and Spycher, N., 2001. Drift-scale coupled processes (DST and THC seepage) models, MDL-NBS-HS-000001 REV01 ICN01. Bechtel SAIC Company (BSC), Las Vegas, Nevada.

Spycher, N.F. and Reed, M.H., 1992. Microcomputer-based modeling of speciation and water-mineral-gas reactions using programs SOLVEQ and CHILLER. In: Proceedings of the 7th International Symposium on Water-Rock Interaction, WRI-7, Park City, Utah, 13–18 July 1992, Kharaka, Y.K. and Maest, A.S., eds., A.A. Balkema, Rotterdam, The Netherlands, v. 2, pp. 1087–1090.

Steefel, C.I. and Lasaga, A.C., 1994. A coupled model for transport of multiple chemical species and kinetic precipitation/dissolution reactions with application to reactive flow in single phase hydrothermal systems. Am. J. Sci., 294: 529-592.

Xu, T. and Pruess, K., 1998. Coupled modeling of non-isothermal multiphase fluid flow, solute transport and reactive chemistry in porous and fractured media: 1. Model development and validation. Lawrence Berkeley National Laboratory Report LBNL–42050, Berkeley, California.

Xu, T. and Pruess, K., 2001a. Modeling multiphase non-isothermal fluid flow and reactive geochemical transport in variably fractured rocks: 1. Methodology. Am. J. Sci., 301: 16–33.

Xu, T. and Pruess, K., 2001b. On fluid flow and mineral alteration in fractured caprock of magmatic hydrothermal systems. J. Geophys. Res., 106 (B2): 2121–2138.

Table 1. Model mineralogy of the middle nonlithophysal zone of the Topopah Spring Tuff (unit tsw34 matrix from Attachments 1 and 2 of Sonnenthal and Spycher, 2001). Quantitative XRD measurements (Carey, 2000) of 4 samples of this unit from core hole SD-9 (depths of 228.6, 237, 244.3, and 251.2 m) and feldspar microprobe analyses were used to derive end-member mineral abundances. Proportions of smectite end-members were estimated by assuming equilibrium with Yucca Mountain pore water at 25°C. Illite abundance was estimated.

Mineral	**Fraction (vol.)**
K-spar	0.3096
Albite	0.2286
Anorthite	0.0077
Ca-smectite	0.0081
Na-smectite	0.0035
Mg-smectite	0.0081
K-smectite	0.0035
Illite	0.0026
Tridymite	0.0489
Cristobalite	0.2588
Quartz	0.1202
Hematite	0.0004
Total	**1.0000**

Table 2. Measured and simulated fluid compositions of plug flow effluent

Fluid type	pH (units)	Total Alkalinity (mg/L as $CaCO_3$)	Silica (mg/L)	Sodium (mg/L)	Potassium (mg/L)	Calcium (mg/L)
Measured steady-state (avg. of 16)	8.4	30	92	11	5	0.25
Final measured composition (63.8 days)	8.2	21	86	9.3	4.5	0.4
Simulation 1 final composition	6.1 (8.1)	94	81	10.4	6.3	0.64
Simulation 2 final composition	5.8	94	48	5.3	5.2	0.32
Simulation 3 final composition	6.1	94	82	10.8	6.2	0.68
Simulation 4 final composition	6.2	94	96	10.7	10.7	0.68
Simulation 5 final composition	6.2	94	96	10.7	10.7	0.68

All other analytes (aluminum, iron, fluoride, chloride, nitrate, sulfate) were below analytical detection limits. Measured values determined at 20°C, simulated values calculated at 94°C. Value in parentheses represents pH corrected for degassing and cooling to 20°C using SOLVEQ v1.0 (see text).

Table 3. Summary table of tuff dissolution simulations

Simulation #	T, P density correction of fluid applied to surface area calculation	Grain size (μm)	Potassium feldspar representation	Representation of clay minerals
1	no	60	Parameter set 1	Ca, Mg, Na, K smectites, illite
2	no	120	Parameter set 1	Ca, Mg, Na, K smectites, illite
3	yes	60	Parameter set 1	Ca-Mg-Na smectite solid solution, illite (K-smectite omitted)
4	yes	60	Parameter set 2	Ca-Mg-Na smectite solid solution, illite (K-smectite omitted)
5	yes	60	Parameter set 2	Ca-Mg-Na smectite solid solution, illite (K-smectite as illite)

Table 4. Comparison of experimental and potential Yucca Mountain repository conditions for fracture sealing

Feature	Experimental Conditions[1]	Potential Yucca Mountain System[2]
Thermal gradient	158°C/m	0.75°C/m
Fracture fluid flux	6×10^{-4} m/s	3×10^{-7} to 3×10^{-8} m/s
Fracture aperture	31 μm	10-1,000 μm
Fluid SiO_2 content	92 mg/L	58-139 mg/L

[1] – Experimental conditions as specified from this study

[2] – Yucca Mountain conditions taken from Sonnenthal and Spycher, 2001

Fracture fluid flux for the Yucca Mountain system was calculated using the following assumptions and values: a long-term infiltration rate of 10 mm/y, a fracture porosity of 0.1 to 1.0% (Freifeld, 2001), and that all of the infiltrating water flows through the fracture network.

Figure Captions

Figure 1. Schematic of dissolution/precipitation experiment.

Figure 2. Comparison of measured values and simulated results of effluent from tuff dissolution column. Plots show variation with time for (a) SiO_2, and (b) Na.

Figure 3. Opened fracture faces at conclusion of fracture sealing experiment. Enhanced image shows fracture temperature profile and fluorescing precipitate (light shades) under ultraviolet illumination on both fracture faces. Vertical dimension is 0.317 m.

Figure 4. Bridging structures (identified with arrows): (a) extending outward from flat fracture face; (b) spanning aperture in cross-cutting natural fracture. Scale bars are 0.5 mm.

Figure 5. Temperature and volume fraction of amorphous silica vs. depth for Simulation B (amorphous silica controlled by kinetic precipitation and dissolution) at 2.51 and 5.01 days. The base of the boiling and silica precipitation fronts move downward as the experiment proceeds due to increasing pressure caused by reduction of fracture aperture.

Figure 6. Porosity vs. depth for simulated fracture-sealing experiments. Simulation A had amorphous silica under equilibrium control, while Simulation B had amorphous silica controlled by kinetic precipitation and dissolution.

Figure 1.

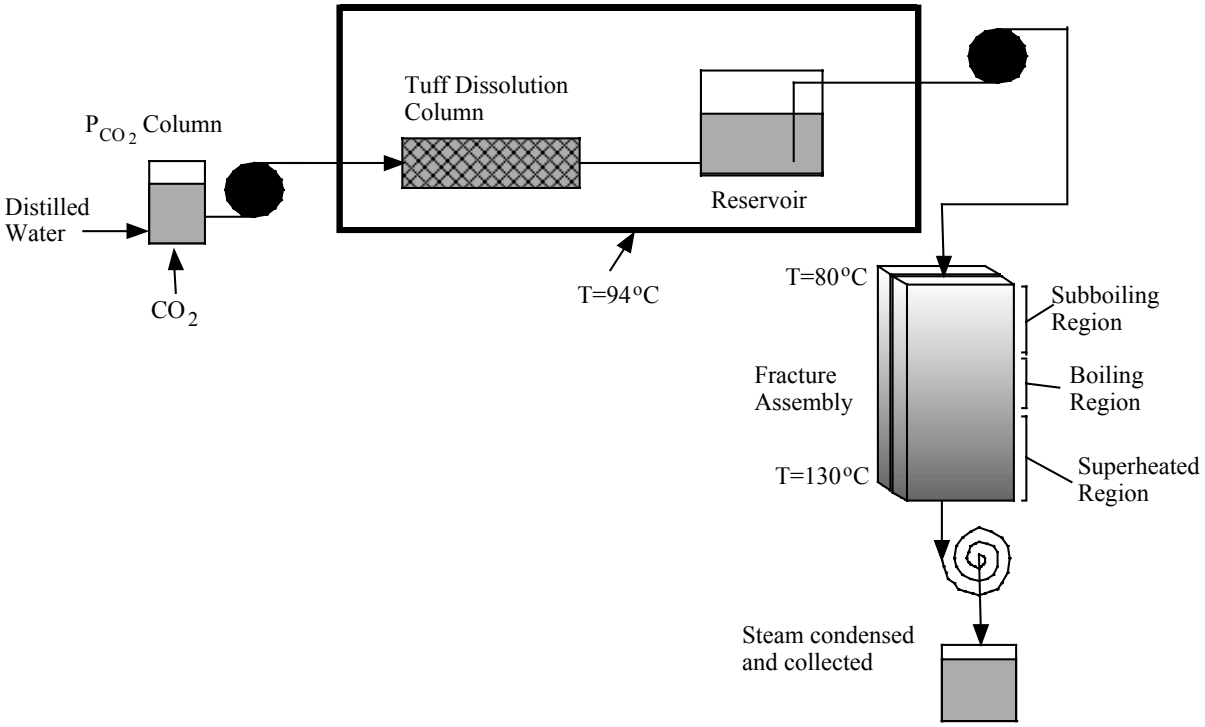
Tuff Dissolution Column
P_{CO_2} Column
Distilled Water
CO_2
Reservoir
T=94°C
T=80°C
Subboiling Region
Fracture Assembly
Boiling Region
T=130°C
Superheated Region
Steam condensed and collected

Figure 2.

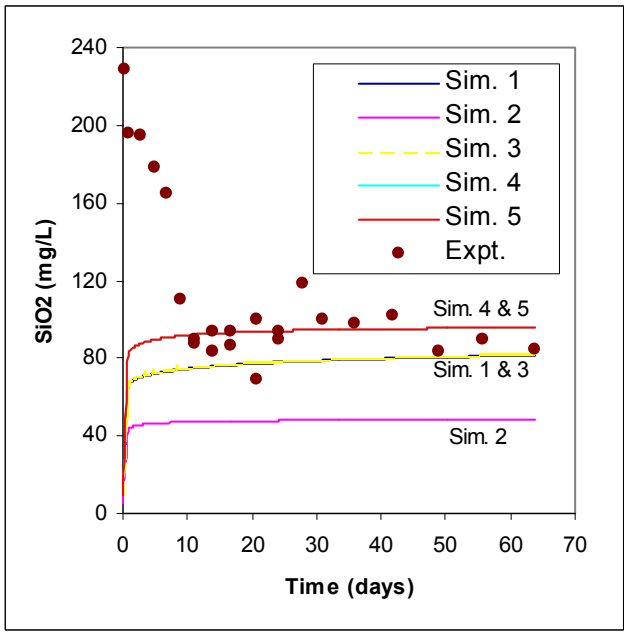
SiO2 (mg/L)
Time (days)
Sim. 1
Sim. 2
Sim. 3
Sim. 4
Sim. 5
Expt.
Sim. 4 & 5
Sim. 1 & 3
Sim. 2

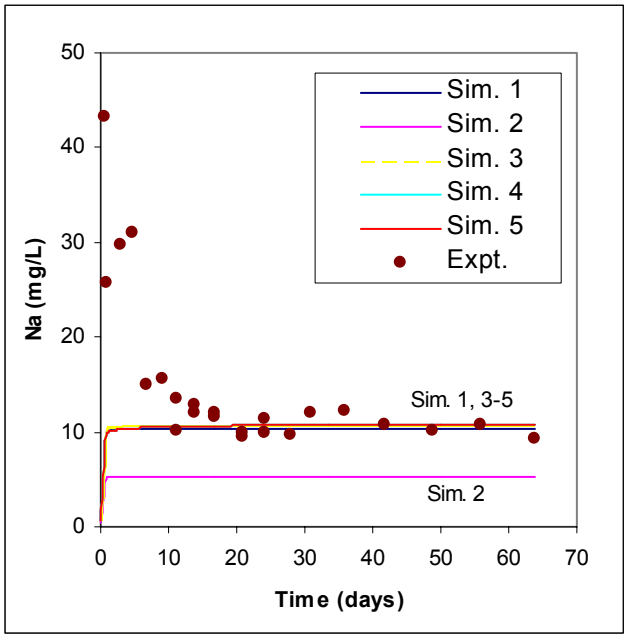
Na (mg/L)
Time (days)
Sim. 1
Sim. 2
Sim. 3
Sim. 4
Sim. 5
Expt.
Sim. 1, 3-5
Sim. 2

Figure 3.

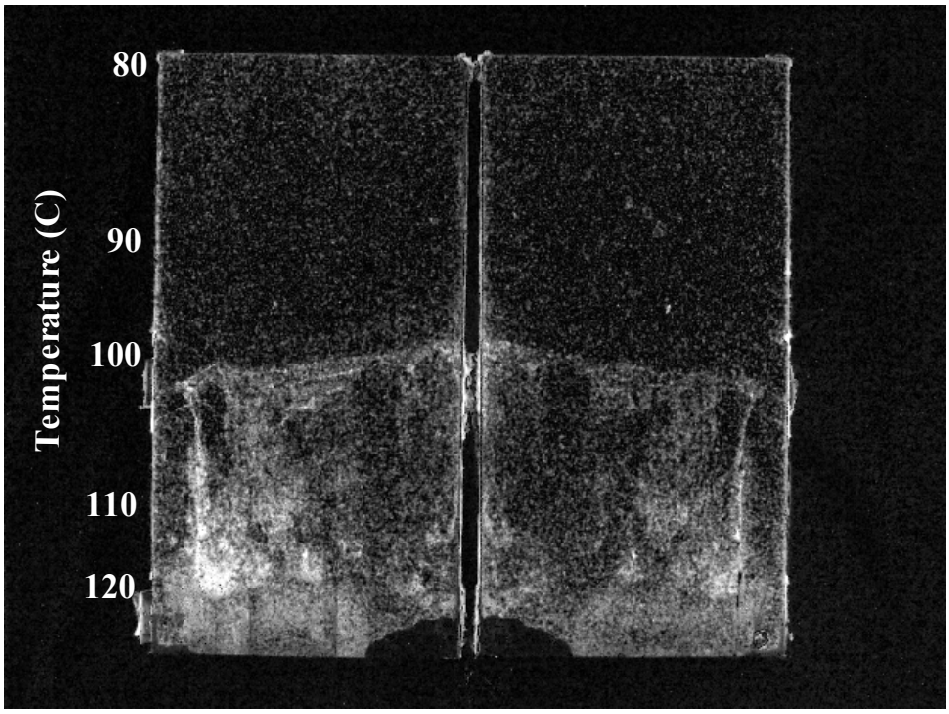

Figure 4.

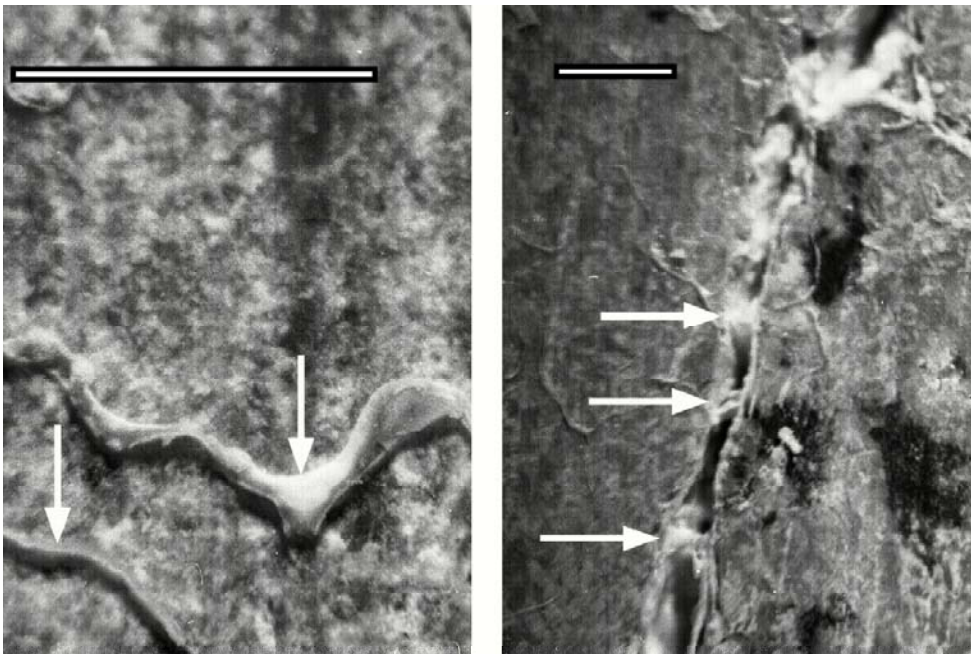

Figure 5.

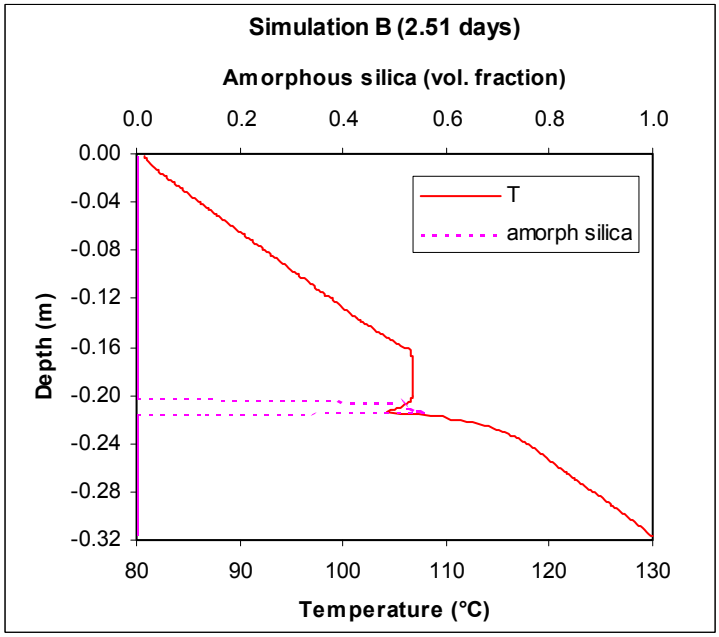
Simulation B (2.51 days)
Amorphous silica (vol. fraction)
0.0
0.2
0.4
0.6
0.8
1.0
0.00
-0.04
-0.08
-0.12
-0.16
-0.20
-0.24
-0.28
-0.32
Depth (m)
T
amorph silica
80
90
100
110
120
130
Temperature (°C)

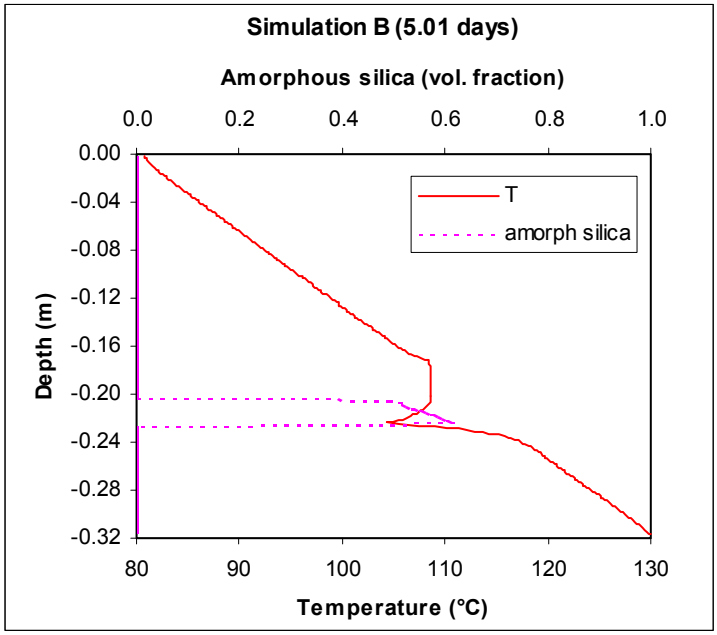
Simulation B (5.01 days)
Amorphous silica (vol. fraction)
0.0
0.2
0.4
0.6
0.8
1.0
0.00
-0.04
-0.08
-0.12
-0.16
-0.20
-0.24
-0.28
-0.32
Depth (m)
T
amorph silica
80
90
100
110
120
130
Temperature (°C)

Figure 6.

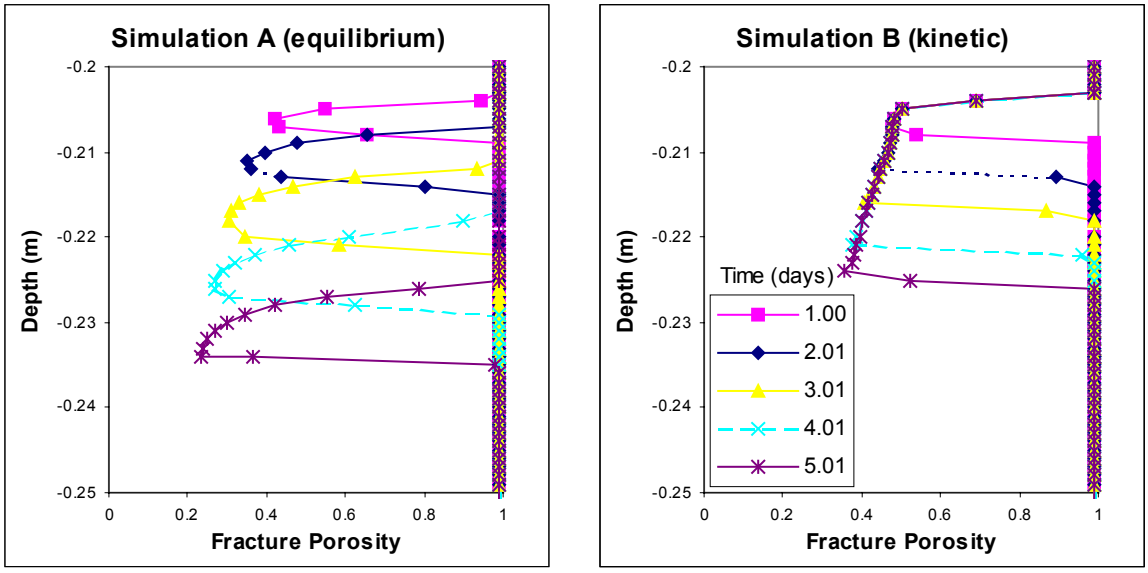
Simulation A (equilibrium)
Depth (m)
-0.2
-0.21
-0.22
-0.23
-0.24
-0.25
0
0.2
0.4
0.6
0.8
1
Fracture Porosity
Simulation B (kinetic)
Depth (m)
Time (days)
1.00
2.01
3.01
4.01
5.01
Fracture Porosity